

A silicon-based widely tunable short-wave infrared optical parametric oscillator

Bart Kuyken,^{1,2,*} Xiaoping Liu,³ Richard M. Osgood Jr.,³ Roel Baets,^{1,2} Günther Roelkens,^{1,2} and William M. J. Green⁴

¹Photonics Research Group, Department of Information Technology, Ghent University–imec, Ghent B-9000, Belgium

²Center for Nano- and Biophotonics (NB-Photonics), Ghent University, Ghent B-9000, Belgium

³Department of Electrical Engineering, Columbia University, New York, New York 10027, USA

⁴IBM T. J. Watson Research Center, Yorktown Heights, New York 10598, USA

*Bart.Kuyken@intec.ugent.be

Abstract: We demonstrate a synchronously pumped optical parametric oscillator (OPO) based on parametric gain in a silicon-on-insulator photonic wire. We exploit the highly nonlinear broadband response of the photonic wire to achieve broadband single-pass amplification up to 54 dB. This allows us to construct an OPO that is tunable across a 75 nm-wide band near 2075 nm, when pumped by a picosecond pulse train at 2175 nm. Additionally we demonstrate broadband tuning across 150 nm by varying the pump wavelength and exploiting the higher order dispersion characteristics of the silicon photonic wire.

©2013 Optical Society of America

OCIS codes: (190.4390) Nonlinear optics, integrated optics; (230.4320) Nonlinear optical devices; (250.5300) Photonic integrated circuits; (140.3550) Lasers, Raman.

References and links

1. K. De Vos, I. Bartolozzi, E. Schacht, P. Bienstman, and R. Baets, "Silicon-on-insulator microring resonator for sensitive and label-free biosensing," *Opt. Express* **15**(12), 7610–7615 (2007).
2. J. T. Robinson, L. Chen, and M. Lipson, "On-chip gas detection in silicon optical microcavities," *Opt. Express* **16**(6), 4296–4301 (2008).
3. J. G. Crowder, S. D. Smith, A. Vass, and J. Keddie, Infrared methods for gas detection," in *Mid-Infrared Semiconductor Optoelectronics* (Springer-Verlag, 2007).
4. E. M. P. Ryckeboer, A. Gassenq, N. Hattasan, B. Kuyken, C. Laurent, R. J. Baptiste, T. Eric, G. Roelkens, W. Bogaerts, and R. Baets, "Integrated spectrometer and integrated detectors on Silicon-on-Insulator for short-wave infrared applications," CTu1A, CLEO, (2012).
5. Y. Huang, S. K. Kalyoncu, Q. Song, and O. Boyraz, "Silicon-on-sapphire waveguides design for mid-ir evanescent field absorption gas sensors," JW2A, CLEO (2012).
6. G. T. Reed and A. P. Knights, *Silicon photonics: an introduction* (John Wiley, 2004).
7. L. Pavesi and D. J. Lockwood, *Silicon photonics*, (Springer, 2004).
8. R. Espinola, J. Dadap, R. Osgood, Jr., S. McNab, and Y. Vlasov, "Raman amplification in ultrasmall silicon-on-insulator wire waveguides," *Opt. Express* **12**(16), 3713–3718 (2004).
9. H. Rong, A. Liu, R. Jones, O. Cohen, D. Hak, R. Nicolaescu, A. Fang, and M. Paniccia, "An all-silicon Raman laser," *Nature* **433**(7023), 292–294 (2005).
10. H. Rong, R. Jones, A. Liu, O. Cohen, D. Hak, A. Fang, and M. Paniccia, "A continuous-wave Raman silicon laser," *Nature* **433**(7027), 725–728 (2005).
11. H. Rong, S. Xu, O. Cohen, O. Raday, M. Lee, V. Sih, and M. Paniccia, "A cascaded silicon Raman laser," *Nat. Photonics* **2**(3), 170–174 (2008).
12. J. I. Dadap, R. L. Espinola, R. M. Osgood, Jr., S. J. McNab, and Y. A. Vlasov, "Spontaneous Raman scattering in ultrasmall silicon waveguides," *Opt. Lett.* **29**(23), 2755–2757 (2004).
13. M. A. Foster, A. C. Turner, J. E. Sharping, B. S. Schmidt, M. Lipson, and A. L. Gaeta, "Broad-band optical parametric gain on a silicon photonic chip," *Nature* **441**(7096), 960–963 (2006).
14. X. P. Liu, R. M. Osgood, Y. A. Vlasov, and W. M. J. Green, "Mid-infrared optical parametric amplifier using silicon nanophotonic waveguides," *Nat. Photonics* **4**(8), 557–560 (2010).
15. B. Kuyken, X. Liu, G. Roelkens, R. Baets, R. M. Osgood, Jr., and W. M. J. Green, "50 dB parametric on-chip gain in silicon photonic wires," *Opt. Lett.* **36**(22), 4401–4403 (2011).
16. B. Kuyken, S. Clemmen, S. K. Selvaraja, W. Bogaerts, D. Van Thourhout, Ph. Emplit, S. Massar, G. Roelkens, and R. Baets, "On-chip parametric amplification with 26.5 dB gain at telecommunication wavelengths using CMOS-compatible hydrogenated amorphous silicon waveguides," *Opt. Lett.* **36**(4), 552–554 (2011).

17. S. K. Selvaraja, P. Jaenen, W. Bogaerts, D. Van Thourhout, P. Dumon, and R. Baets, "Fabrication of photonic wire and crystal circuits in silicon-on-insulator using 193 nm optical lithography," *J. Lightwave Technol.* **27**(18), 4076–4083 (2009).
18. ePIXfab: The Silicon Photonics Platform. <http://www.epixfab.eu/>
19. A. D. Bristow, N. Rotenberg, and H. M. van Driel, "Two-photon absorption and Kerr coefficients of silicon for 850–2200 nm," *Appl. Phys. Lett.* **90**(19), 191104 (2007).
20. R. M. Osgood, Jr., N. C. Panoiu, J. I. Dadap, X. Liu, X. Chen, I.-W. Hsieh, E. Dulkeith, W. M. Green, and Y. A. Vlasov, "Engineering nonlinearities in nanoscale optical systems: physics and applications in dispersion-engineered silicon nanophotonic wires," *Adv. Opt. Photon.* **1**(1), 162–235 (2009).
21. M. A. Foster, A. C. Turner, R. Salem, M. Lipson, and A. L. Gaeta, "Broad-band continuous-wave parametric wavelength conversion in silicon nanowaveguides," *Opt. Express* **15**(20), 12949–12958 (2007).
22. J. D. Harvey, R. Leonhardt, S. Coen, G. K. L. Wong, J. C. Knight, W. J. Wadsworth, and P. St. J. Russell, "Scalar modulation instability in the normal dispersion regime by use of a photonic crystal fiber," *Opt. Lett.* **28**(22), 2225–2227 (2003).
23. Y. Zhou, K. K. Y. Cheung, S. Yang, P. C. Chui, and K. K. Wong, "Widely tunable picosecond optical parametric oscillator using highly nonlinear fiber," *Opt. Lett.* **34**(7), 989–991 (2009).
24. B. Kuyken, X. Liu, R. M. Osgood, Jr., R. Baets, G. Roelkens, and W. M. Green, "Mid-infrared to telecom-band supercontinuum generation in highly nonlinear silicon-on-insulator wire waveguides," *Opt. Express* **19**(21), 20172–20181 (2011).
25. G. P. Agrawal, *Nonlinear Fiber Optics* (Academic Press, 1995).
26. Q. Lin, T. J. Johnson, R. Perahia, C. P. Michael, and O. J. Painter, "A proposal for highly tunable optical parametric oscillation in silicon micro-resonators," *Opt. Express* **16**(14), 10596–10610 (2008).
27. M. Pu, L. Liu, H. Ou, K. Yvind, and J. M. Hvam, "Ultra-low-loss inverted taper coupler for silicon-on-insulator ridge waveguide," *Opt. Commun.* **283**(19), 3678–3682 (2010).
28. P. Dumon, W. Bogaerts, D. Van Thourhout, D. Taillaert, R. Baets, J. Wouters, S. Beckx, and P. Jaenen, "Compact wavelength router based on a Silicon-on-insulator arrayed waveguide grating pigtailed to a fiber array," *Opt. Express* **14**(2), 664–669 (2006).
29. J. F. Bauters, M. J. Heck, D. D. John, J. S. Barton, C. M. Bruinink, A. Leinse, R. G. Heideman, D. J. Blumenthal, and J. E. Bowers, "Planar waveguides with less than 0.1 dB/m propagation loss fabricated with wafer bonding," *Opt. Express* **19**(24), 24090–24101 (2011).
30. J. S. Levy, A. Gondarenko, M. A. Foster, A. C. Turner-Foster, A. L. Gaeta, and M. Lipson, "CMOS-compatible multiple-wavelength oscillator for on-chip optical interconnects," *Nat. Photonics* **4**(1), 37–40 (2010).
31. L. Razzari, D. Duchesne, M. Ferrera, R. Morandotti, S. Chu, B. E. Little, and D. J. Moss, "CMOS-compatible integrated optical hyper-parametric oscillator," *Nat. Photonics* **4**(1), 41–45 (2010).
32. P. Del'Haye, A. Schliesser, O. Arcizet, T. Wilken, R. Holzwarth, and T. J. Kippenberg, "Optical frequency comb generation from a monolithic microresonator," *Nature* **450**(7173), 1214–1217 (2007).
33. C. Y. Wang, T. Herr, P. Del'Haye, A. Schliesser, J. Hofer, R. Holzwarth, T. W. Hänsch, N. Picqué, and T. J. Kippenberg, "Mid-infrared optical frequency combs at 2.5 μm based on crystalline microresonators," *Nat. Commun.* **4**, 1345–1348 (2013).
34. M. Peccianti, A. Pasquazi, Y. Park, B. E. Little, S. T. Chu, D. J. Moss, and R. Morandotti, "Demonstration of a stable ultrafast laser based on a nonlinear microcavity," *Nat Commun.* **3**, 765–767 (2012).

1. Introduction

Although the principal drivers for the dense integration of complex optical functions within the silicon photonics platform have been applications in telecom and datacom, a variety of life science applications are also being pursued. This has led to the demonstration of several compact silicon photonic sensing systems for bio-molecule detection [1] and gas sensing [2]. The majority of sensing systems demonstrated to date operate within the telecom wavelength band. However, in many cases, optical sensing systems would benefit from operating in the mid-infrared (2–10 μm) wavelength region. In this wavelength region, the strong and specific absorption lines of many molecules [3], i.e. their "molecular fingerprints," allow for sensitive and selective spectroscopic analysis of the analyte of interest [4,5].

A tunable silicon light source is a highly important component of a fully integrated silicon photonic integrated circuit platform for these lab-on-chip applications. Development of such a source has been hampered by the indirect bandgap of silicon [6,7], which makes light emission very inefficient. However, the high optical confinement in a silicon photonic wire surrounded by low refractive index materials such as SiO_2 and air can lead to strong nonlinear optical effects. Since silicon is a centro-symmetrical crystal, the third order Kerr nonlinear effect and the Raman nonlinearity are dominant. In fact, the strong Raman effect has been used to demonstrate amplification and lasing in silicon in the telecom band [8–10] as well as

in the short-wave infrared [11] through cascaded Raman amplification. However, because of the inherently limited bandwidth of the Raman gain (105 GHz) [12] in crystalline silicon, it is difficult to make these devices widely tunable. In contrast, the Kerr effect does not have this disadvantage. For example, a number of broadband silicon-based parametric amplifiers have been demonstrated, in crystalline [13–15] and hydrogenated amorphous [16] Si waveguides. In this paper we report a widely tunable light source by exploiting the large Kerr nonlinearity of dispersion-engineered silicon photonic wires, using four-wave mixing (FWM). We demonstrate a pulsed short-wave infrared optical parametric oscillator (OPO) which is continuously tunable over 75 nm in a band around 2075 nm, and over 25 nm in a band around 2275 nm, for a fixed pump wavelength of 2175 nm. By utilizing the silicon waveguide dispersion we succeed in tuning the oscillation wavelength of the OPO over more than 150 nm, by tuning the pump over only 55 nm. This demonstration is an important step towards tunable light sources fully integrated in silicon.

2. Device structure

The core of the OPO consists of a highly nonlinear silicon photonic wire. The photonic wire is fabricated in a CMOS pilot line [17, 18] on a 200 nm silicon-on-insulator (SOI) wafer, consisting of a 220 nm silicon waveguide layer on top of a 2 μm buried oxide layer. Figure 1 (a) shows a schematic cross section of the silicon photonic wire. The 2 cm-long air-clad photonic wire has a rectangular cross-section of 900 nm x 220 nm. The photonic wire is terminated by an adiabatic taper at both ends, transitioning to a 3 μm wide waveguide section at the cleaved facets. By using a cut-back technique on a set of 0.07, 1, 2, 4, 7 cm long wires, the propagation loss for the quasi-TE mode is determined to be 1 ± 0.1 dB/cm across the 2100–2400 nm wavelength range. Input/output coupling is accomplished with lensed fibers, resulting in a -7 dB \pm 1 dB coupling efficiency at each facet. The high index contrast between the silicon core and its cladding allows the 2 cm-long wire to be coiled into a small spiral occupying only 700x400 μm^2 , as shown in Fig. 1(b).

The high intrinsic Kerr nonlinearity of silicon ($\chi^{(3)} \sim 3.9 \times 10^5$ pm²/V² at 2200 nm [19]) as well as the high optical confinement obtained in these photonic wires (effective mode area of 0.27 μm^2) produces a large real part of the complex effective nonlinear parameter γ . For the quasi-TE mode, γ is approximately $(150 + i0.6)/\text{W}\cdot\text{m}$ [20] within the 2150–2200 nm (~ 0.56 eV) wavelength range. The photonic wires are pumped near 2200 nm in order to minimize parasitic two-photon absorption processes in silicon (1.12eV bandgap), resulting in a large nonlinear figure of merit $\text{Re}\{\gamma\}/(4\pi\text{Im}\{\gamma\}) \sim 20$. The efficiency of the FWM process is further enhanced by phase matching the optical waves, achieved by engineering the photonic-wire dispersion. The phase-matching condition in a degenerate FWM process is given by [21]

$$\beta_2 \Delta\omega^2 + \frac{1}{12} \beta_4 \Delta\omega^4 + 2\gamma P = 0 \quad (1)$$

Here, $\Delta\omega$ is the frequency detuning between pump and signal (and also between pump and idler), β_2 and β_4 are the second- and fourth-order dispersion coefficients respectively, evaluated at the pump frequency ($\beta_n = \left. \frac{d^n \beta}{d\omega^n} \right|_{\omega_p}$). This relation yields a solution in the vicinity

of the pump (i.e., where the fourth-order dispersion term is negligible) when the second-order dispersion is negative (anomalous dispersion), leading to so-called broadband phase matching. Far from the pump, a second solution (termed discrete-band phase matching) can be found provided that the sign of the fourth-order dispersion is opposite to the sign of the second-order dispersion. This discrete band phase matching principle has been used to obtain amplification in photonic crystal fiber [22] and oscillation in highly nonlinear optical fiber [23], while pumping the fiber within the normal dispersion regime. The photonic wire used here permits both broadband and discrete band phase matching, since it has a negative

second-order dispersion coefficient $\beta_2 \sim -0.6 \text{ ps}^2/\text{m}$ and a positive fourth-order dispersion coefficient $\beta_4 \sim 5.1 \times 10^{-4} \text{ ps}^4/\text{nm}$ at 2175 nm for the quasi-TE mode, as experimentally measured in [24].

3. Single-pass parametric fluorescence and gain

In the absence of a probe signal, the high peak-power pump pulses will amplify background noise within the highly nonlinear silicon wire [15]. This process is commonly referred to as modulation instability (MI) and/or parametric fluorescence [25], and can be seen in Fig. 1(c). The black trace illustrates the spectrum of the picosecond pump pulse train (Coherent Mira-OPO, FWHM = 2 ps, repetition rate = 76 MHz, peak power $\sim 24 \text{ W}$, center wavelength of 2160 nm) at the input of the wire, as recorded by a mid-IR spectrum analyzer (Yokogawa AQ6375) at a resolution bandwidth of 1 nm. The red trace is obtained after transmission of the pump through the quasi-TE mode of the 2 cm-long wire. Near the center wavelength of the pump, two side lobes at 2062 nm and 2260 nm (labeled MI (1)) appear in the output spectrum. These side lobes relate to the first set of phase-matching solutions of Eq. (1), nearest to the pump frequency. Further away from the pump, an additional lobe labeled MI (2) appears at 1835 nm. At this wavelength Eq. (1) is also satisfied, leading to a discrete

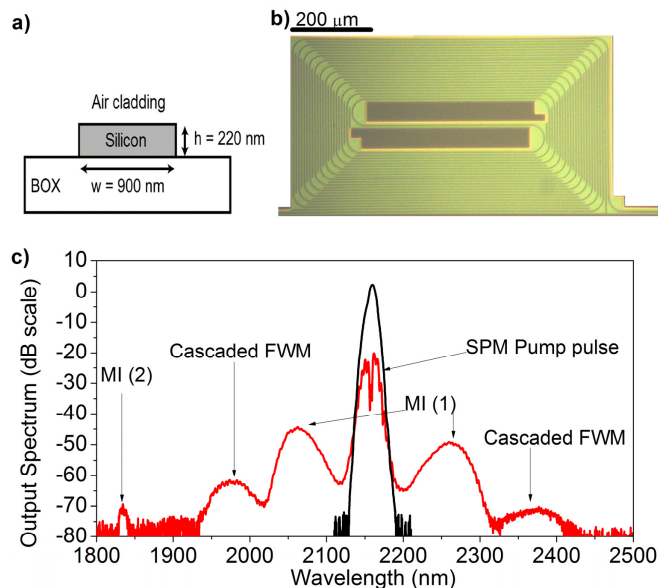


Fig. 1. (a) Schematic cross-section of the silicon photonic wire. (b) Optical microscope image of the spiral-coiled 2 cm-long silicon wire used within the OPO. The on-chip footprint occupied by the wire is $700 \mu\text{m} \times 400 \mu\text{m}$. (c) The input (black trace) and output (red trace) spectra of the picosecond pump pulses (repetition rate = 76 MHz, FWHM = 2 ps, peak power $\sim 24 \text{ W}$) centered around 2160 nm, going through the 2 cm silicon photonic wire. The pump is broadened by self-phase modulation. The spectral peaks MI(1) and MI(2) label the phase matched wavelengths at which the pump amplifies the background noise via modulation instability.

phase matching band. From photon energy conservation considerations, an MI (2) peak is also expected near 2620 nm. However this is beyond the cut-off wavelength of the optical spectrum analyzer (OSA) used. Finally, two additional peaks appear at 1975 nm and 2378 nm, originating from cascaded FWM processes between the pump and the MI (1) sidelobes.

The strong modulation instability sidelobes in Fig. 1(c) mark the spectral regions in which phase matching is achieved, and accordingly label the locations where optical parametric amplification is expected. The magnitude of the on-chip single-pass parametric gain is measured via the amplification experienced by a low power continuous wave (CW) probe

signal (IPG Photonics $\text{Cr}^{2+}:\text{ZnSe}$ external cavity tunable laser), as described in [14]. The picosecond pump operating at a wavelength of 2175 nm is coupled into the quasi-TE mode of the wire, with 48 pJ pulses (peak power ~ 24 W) at the wire input. The pump is combined with the co-polarized low-power probe laser (< 0.1 mW), using a 90%/10% fused fiber coupler. Figure 2 illustrates that the measured single-pass gain can be as large as 54 dB (black squares) for a probe signal tuned to 2275 nm (MI (1) band on the red side of the pump), while the corresponding on-chip conversion efficiency (red circles) has a maximum value of 58 dB at 2083 nm. The single-pass gain within the MI (2) bands could not be directly measured, due to the absence of an appropriate optical probe source at either 1835 nm or 2620 nm.

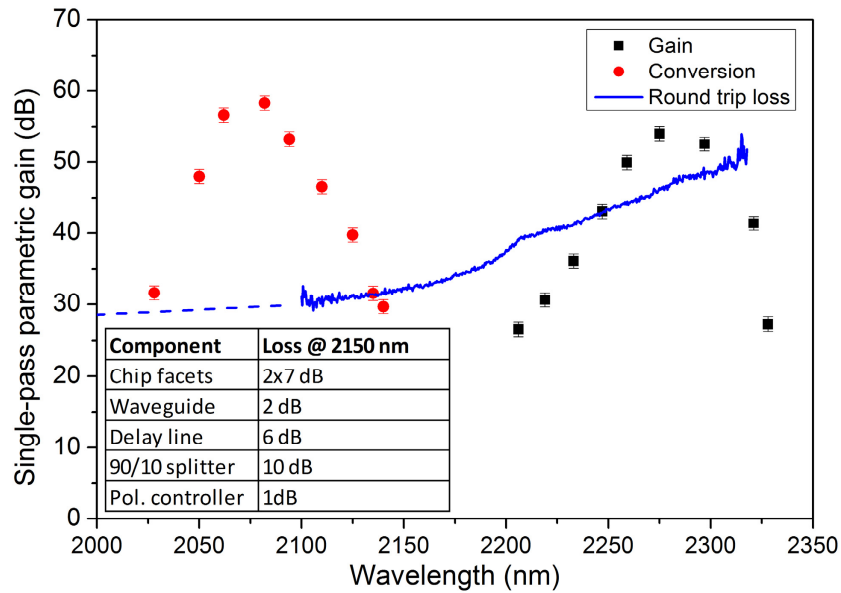


Fig. 2. The on-chip single-pass parametric gain and conversion of a low-power CW signal (< 0.1 mW) within the 2 cm long silicon photonic wire. A CW probe signal is combined with a high peak power picosecond source (repetition rate = 76 MHz, FWHM = 2 ps), having an on-chip peak power of 24 W (48 pJ pulse energy). The error bars are determined by the ± 1 dB uncertainty in the input/output coupling efficiency. The round-trip loss of the fiber-based cavity is shown in blue. Due to the absence of appropriate optical sources below 2100 nm, the values between 2000 nm and 2100 nm (dashed blue curve) are a linear extrapolation of the round-trip loss to the value obtained at 1550 nm. The inset table shows the contribution of the fiber loop components to the total round-trip loss at 2150 nm.

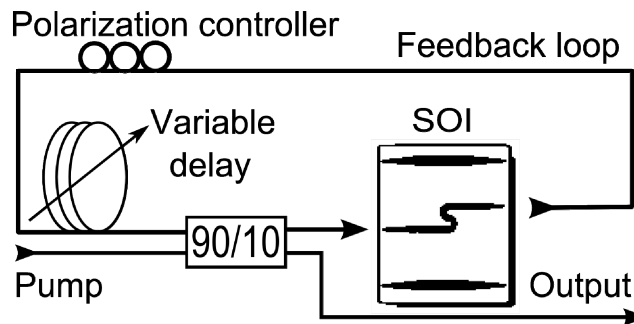


Fig. 3. Schematic of the fiber cavity configuration of the silicon based OPO. The pump pulses are combined with the output of the silicon chip with a 90/10 coupler. A variable delay line within the cavity ensures that the round-trip time of the signal pulses matches the pump repetition period. A polarization controller ensures that the light within the feedback loop is coupled into the TE mode of the waveguide.

4. Optical parametric oscillation

The optical feedback required for the parametric oscillator is achieved using a fiber cavity configuration consisting of ~ 5.8 m standard single mode fiber (SMF-28), as illustrated in Fig. 3. The output from the amplifying silicon photonic wire is combined with the pump pulses using a 90% (pump) / 10% (signal) fused fiber coupler and directed back to the wire input facet. The feedback loop contains a variable delay line to synchronize the cavity circulating pulses with the input pump pulses. When the cavity round-trip time is an integer multiple of the pulse repetition period (two times in this work), the circulating generated signals will overlap temporally and spatially with the pump pulse train inside the silicon photonic wire. Therefore, the circulating pulses will be synchronously amplified each round-trip, resulting in optical parametric oscillation provided that the gain exceeds the round-trip loss. We note that parametric amplification within the optical fiber cavity is negligible since the nonlinear parameter of SMF-28 fiber is approximately five orders of magnitude smaller than that of the silicon waveguide.

The measured round-trip loss of the cavity, illustrated by the blue curve in Fig. 2, originates from the high fiber-chip insertion losses and the insertion loss of the fiber-optic components within the system. The intracavity round-trip losses at 2150 nm are tabulated in the inset of Fig. 2. The total round-trip loss is found to increase from 32 dB at 2100 nm, to 37 dB at 2200 nm, and to 48 dB at 2300 nm. The large single-pass parametric gain available in the silicon photonic wire can compensate for the high round-trip losses in two spectral bands near 2075 nm and 2275 nm; thus optical parametric oscillation can occur within these bands.

The output spectrum of the silicon-based OPO pumped at 2175 nm is shown in Fig. 4(a). When the OPO is pumped below threshold, i.e. on-chip pump pulse energy < 15 pJ (see Fig. 4(b)), a broadband modulation instability spectrum is generated. At higher pump energies, the single-pass parametric gain overcomes the round-trip loss in the fiber cavity, and oscillation occurs. In Fig. 4(a), the spectrum of the output pulse train centered near 2078 nm becomes apparent above threshold. When the OPO is pumped at 43.1 pJ the 3 dB optical bandwidth of the output pulse is 7.5 nm. The on-chip output pulse energy, defined as the generated signal pulse energy at the output end of the photonic wire, is plotted as a function of the on-chip pump pulse energy in Fig. 4(b). The parametric oscillation threshold occurs at approximately 15 pJ. The optical pulses reach a peak on-chip pulse energy of 1.52 pJ for an on-chip pump

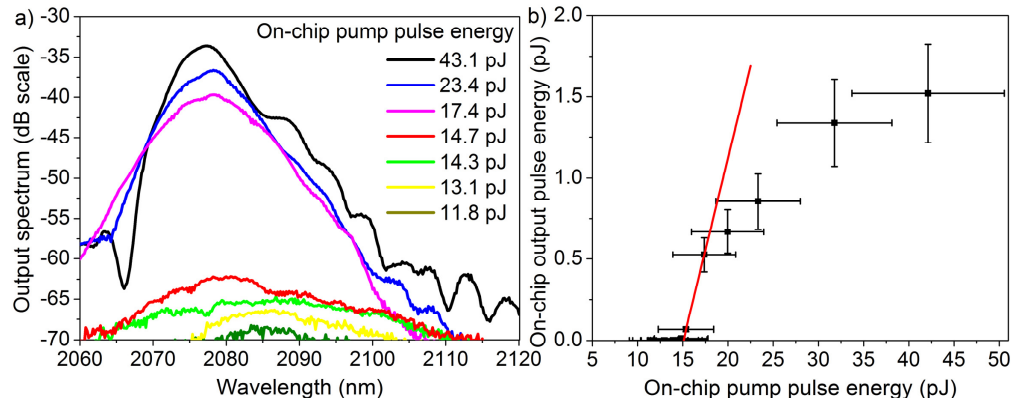


Fig. 4. (a) The output spectrum of the OPO as a function of on-chip pump pulse energy (documented in the legend). The pump wavelength is 2175 nm. At an on-chip pump energy of 43.1 pJ the 3 dB spectral width of the generated pulses is 7.5 nm. (b) On-chip output energy of the generated pulses as a function of the on-chip pump pulse energy, demonstrating an oscillation threshold of ~ 15 pJ and a slope efficiency of $22.6 \pm 4\%$, for a pump at 2175 nm. Using 43.1 pJ pump pulses, the OPO generates 1.52 pJ pulses on-chip. The error bars are determined by the ± 1 dB uncertainty in the input/output coupling efficiency.

pulse energy of 43.1 pJ. The on-chip slope efficiency at threshold is $22.6 \pm 4\%$. In the absence of nonlinear loss, the maximum theoretically expected on-chip slope efficiency, for which all additional pump photons at the input of the wire are converted to signal and idler photons at the output of the wire, is given by

$$\frac{\hbar\omega_s}{2\hbar\omega_p}\exp(-\alpha L) = 33.1\% \quad (2)$$

where ω_s is the signal frequency, ω_p the pump frequency, \hbar Planck's constant, α the linear loss of the silicon photonic wire, and the L the wire length. The discrepancy between the theoretical and experimental values can be explained in terms of an excess nonlinear loss from residual two-photon absorption at the pump wavelength, as well as from absorption due to the associated free-carriers. The nonlinear loss also makes the OPO round-trip loss pump-power dependent, such that the on-chip output pulse energy is not linearly dependent upon the on-chip input pump pulse energy.

The round-trip time in the fiber cavity depends upon the generated signal wavelength, on account of the dispersion accumulated after propagation through the optical fiber and the silicon photonic wire. The net dispersion contribution of the silicon photonic wire is significantly smaller than that of the fiber feedback loop due to its relatively short length and due to the low dispersion designed into the waveguide. Therefore, by changing the optical path length of the fiber feedback loop, a range of signal wavelengths can be synchronized to temporally and spatially overlap with the pump pulse train, resulting in tunable parametric oscillation. The variable delay line within the fiber cavity can be used to continuously tune the OPO output wavelength, provided that the single-pass-gain exceeds the round-trip loss. As illustrated by the data in Fig. 2, oscillation is expected within two bands near 2075 nm and 2275 nm, respectively. Figure 5 plots the on-chip output pulse energy of the OPO as a function of output wavelength, selected using the variable delay line. The pump wavelength is 2175 nm, and the on-chip pump pulse energy is 48 pJ. The figure illustrates that the OPO can be tuned across a bandwidth of 75 nm near the peak on-chip pulse energy wavelength of 2087 nm. The on-chip pulse energy decreases on either side of this peak due to decreasing single-pass gain. Figure 5 also plots the on-chip output energies obtained for OPO operation in the band near 2275 nm. However, the maximum on-chip output power within this wavelength range is approximately 10x lower than that near 2087 nm, on account of the larger round-trip losses shown in Fig. 2. The inset of Fig. 5 shows several output spectra obtained while tuning the OPO across the band near 2075 nm.

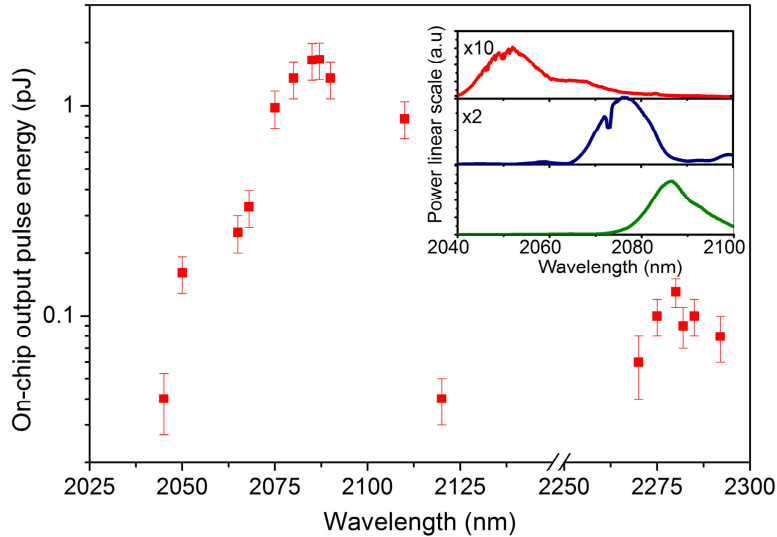


Fig. 5. On-chip output energy of the generated pulses as a function of oscillation wavelength, for an on-chip pump pulse energy of 48 pJ at 2175 nm. The synchronized output wavelength is tuned using the variable delay line within the fiber cavity. The larger round-trip loss in the cavity leads to lower output at longer wavelengths near 2275 nm. The error bars are determined by the ± 1 dB uncertainty in the input/output coupling efficiency. The inset plots output spectra obtained for three different settings of the delay line, demonstrating tunable oscillation at three different wavelengths. In comparison with the green trace, the power scale of the blue trace has been magnified by a factor of two, and the scale of the red trace by a factor of 10.

As mentioned above, Eq. (1) has another set of solutions far from the pump wavelength, i.e. those from discrete phase matching. As an example, Fig. 1(c) illustrates that for pump pulses centered at a wavelength of 2160 nm, an additional modulation instability peak near 1835 nm (MI(2)) is visible. When the pump is centered at 2180 nm, this discrete band shifts to 1857 nm, where phase matching (and thus amplification) is obtained. Oscillation in this band is obtained by changing the cavity round-trip time to be synchronous for pulses generated at 1857 nm. The output spectrum of the OPO operating in this mode is illustrated by the black trace in Fig. 6. This discrete band phase matching not only increases the operational bandwidth of the OPO, but it also provides an alternative method of tuning the output wavelength over a broad wavelength range. The frequency detuning $\Delta\omega$ far from the pump, where Eq. (1) is satisfied, depends strongly upon the value of the fourth-order dispersion coefficient β_4 , which is itself wavelength-dependent. By shifting the pump wavelength, both $\Delta\omega$ and β_4 are varied, and the wavelength for which discrete band phase matching occurs is tuned. A set of output spectra taken with different pump wavelengths is shown in Fig. 6. Continuous tuning across 150 nm (12.4 THz) from 1857 nm to 2009 nm is obtained by tuning the pump wavelength by only 55 nm (3.38 THz), from 2180 nm to 2235 nm. Optimizing the geometry of the photonic wire to obtain normal dispersion with negative fourth-order dispersion can ultimately lead to even more broadband tuning, with a smaller change in the pump wavelength [26]. Moreover, for the same pump tuning range, the four-wave mixing process simultaneously generates an idler at wavelengths from 2634 nm to 2507 nm. However, the idler lies outside the range of the optical spectrum analyzer used in the experiment and could therefore not be observed.

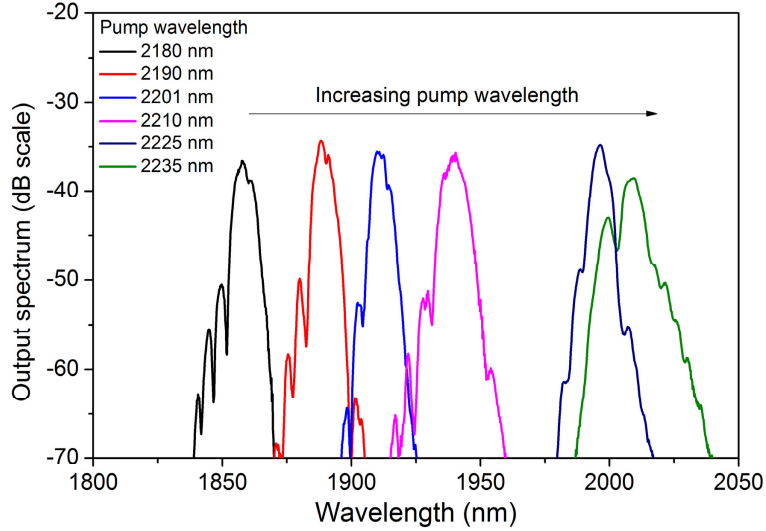


Fig. 6. Output spectrum of the optical parametric oscillator operating with discrete-band phase matching. The on-chip pump pulse energies (wavelengths) used are 48.4 pJ (2180 nm), 27.0 pJ (2190 nm), 23.4 pJ (2201 nm), 18.8 pJ (2210 nm), 19.0 pJ (2225 nm) and 16.4 pJ (2235 nm). Continuous tuning across a 150 nm spectral range is obtained.

As shown in Fig. 7, the threshold on-chip pump-pulse energy is 16.4 pJ for a pump at 2235 nm generating a signal at 1995 nm. The slope efficiency at threshold is $41 \pm 8\%$, while a value of 35.3% is theoretically expected from Eq. (2). Although these values agree within error, the discrepancy in the mean slope efficiency can be seen to originate from the experimental uncertainty in the wire input/output coupling, which impacts estimation of the on-chip pulse energies. In Fig. 7, the on-chip output pulse energy is linearly dependent upon the on-chip input-pulse energy. From these findings we can conclude that the nonlinear absorption is negligible when the OPO is pumped at 2235 nm, at least within the range of on-chip pump pulse energies accessible experimentally.

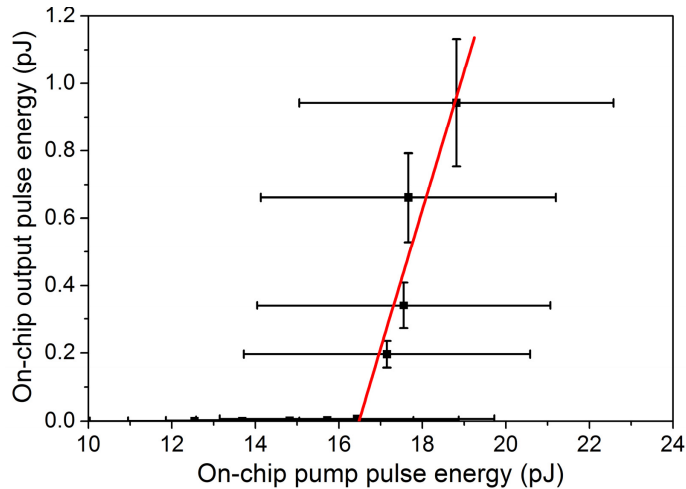


Fig. 7. On-chip output pulse energy as a function of the on-chip pump-pulse energy, for a pump wavelength of 2235 nm generating an OPO signal at 1995 nm. The threshold on-chip pump energy is 16.4 pJ, and the slope efficiency is $41 \pm 8\%$. Using 18.8 pJ pump pulses, the OPO generates 0.94 pJ pulses on-chip. The error bars are determined by the ± 1 dB uncertainty in the input/output coupling efficiency.

5. Conclusion

In summary, we have demonstrated a widely tunable optical parametric oscillator based upon four-wave mixing in a silicon photonic wire. High single-pass broadband optical parametric gain (up to 54 dB) is achieved in a 2 cm long silicon photonic wire when it is pumped with on-chip pump pulses of 48 pJ at 2175 nm. Enclosing the chip within a fiber loop cavity, the high optical gain exceeds the round-trip losses, leading to a synchronously pumped silicon-based OPO. By varying the round-trip time within the fiber cavity, the OPO center wavelength can be tuned across a 75 nm bandwidth near 2075 nm. Furthermore, by taking advantage of the wavelength-dependent higher-order dispersion of the silicon photonic wire, the output wavelength of the OPO can also be tuned from 1857 nm to 2009 nm, by changing the pump wavelength over only 55 nm from 2180 nm to 2235 nm.

This silicon-based OPO represents an important step towards a widely tunable monolithically integrated silicon source. Improved performance can be achieved by increasing the input/output coupling efficiency to the chip using inverted taper structures [27], and by incorporating custom-designed silicon photonic wavelength (de)multiplexing structures for combining/splitting the pump and signal beams with low loss [28]. Further improvement can be obtained by integrating the feedback loop on-chip, for example by using low-loss silicon nitride waveguides [29]. The thermo-optic effect can then be used on-chip to tune the round-trip time and thus the signal wavelength. Such developments could ultimately result in the miniaturization of large bench-top optical parametric oscillators into highly efficient chip-scale light sources. A promising alternative approach is to make use of integrated high-quality ring resonators pumped with continuous-wave lasers, to enable construction of all-silicon optical frequency comb generators through cascaded four-wave mixing [30–33]. Another application of such ring resonators could be the generation of ultra-low-noise mode-locked lasers by means of filter driven four-wave mixing [34].

Acknowledgments

This work was supported by the FP7-ERC-MIRACLE and FP7-ERC-InSpectra project. Bart Kuyken acknowledges a scholarship provided by the Fund for Scientific Research Flanders (FWO-Vlaanderen). Richard Osgood and Xiaoping Liu acknowledge support from a National Science Foundation (NSF)/Engineering and Physical Sciences Research Council (EPSRC) Materials World Network Program Grant (DMR#-MWN-0806682).